Finite element analysis of the viscous flow in a vaned radial diffuser

Rita J. Schnipke, James G. Rice, and Ronald D. Flack*

A new finite element method was used to analyze an experimental model of a radial vaned diffuser. The new method includes a streamline upwind formulation for the advection terms in the governing equations. The streamline upwind significantly reduces numerical diffusion while maintaining the stability of the conventional upwind formulation. The new finite element method also incorporates an iterative equal-order, velocity-pressure solution method based on the well-known SIMPLER algorithm. The results of the analysis are compared to flow visualization studies of the experimental model. The flow separation point for the four blade diffuser was predicted to occur at 19, 6% of the blade length from the leading edge. The experimentally determined value was 23% of the blade length. For the eight blade diffuser model, separation was predicted to occur at 43% of the blade length from the leading edge, as compared to the experimentally observed value of 50% of the blade length. With this performance comparison, the proposed finite element method has been demonstrated to be reliable for predicting complex fluid flows.

Keywords: *numerical methods; computational fluids; finite element; turbomachinery; numerical diffusion*

Introduction

The diffuser in a turbomachine converts a portion of the fluid's kinetic energy into static pressure. A vaned diffuser uses blades to better guide the flow to obtain a higher rate of diffusion than is possible with a vaneless diffuser.

An ideal diffuser design will provide efficient pressure recovery over a wide range of flow conditions; however, this is rarely achieved in practice. Most turbomachine designs are based on limited empirical data. Numerical methods offer the potential to provide parametric studies for the designer to maximize the performance of the turbomachine. Before the numerical methods can be used with confidence, they must be verified by comparing numerical predictions to measured data.

To this end, a clear plastic model of a radial vaned diffuser was designed and built at the University of Virginia[1] (see Figure 1). The purpose of the model was to study the flow patterns for various blade designs in the diffuser. The design also allows for detailed measurements of velocities in the diffuser, thus providing experimental data for verification of computational fluid dynamics models. For a more detailed description of the experimental diffuser model, see Reference 1.

This experimental diffuser model was chosen as an application for the new computational method presented here for several reasons. First, the diffuser model was designed for two-dimensional flow. Since the method used here departs significantly from many of the current finite element flow models, a two-dimensional version was developed to reduce debugging efforts and demonstrate the method's reliability.

Another reason this diffuser rig was chosen was that the fluid flow in the rig involves several complex features. The flow contains large separation regions, areas of steep velocity, and pressure gradients and represents a high Reynolds number. All these features provide difficulties for any computational method. Hence, successfully modeling these features would demonstrate the robustness of the presented finite element method.

Finally, the diffuser model was designed so that laser velocimetry measurements could be taken. These data would provide a means of verifying the accuracy of the finite element method proposed here. As a preliminary step to this exacting verification process, the new finite element method's predicted results will be compared to the flow visualization results of the experimental diffuser model reported in Brownell *et al.*[1] The comparison to the laser velocimetry data will be published subsequently.

This new finite element method was designed to incorporate the best features of both finite difference and finite element methods. To date, most finite element methods for fluid flow have required far more computer storage than finite difference methods and were limited in the types of problems that they could readily solve. From the onset, the current method was developed to be competitive in applications, computer storage, and execution times with the more popular finite difference methods. However, the new method is a finite element formulation, thus taking advantage of the inherent geometric flexibility of finite elements.

In the following sections, we outline the proposed finite element method. Following that description, we present the diffuser geometry. Next, we discuss the predicted results along with the comparison to the flow visualization studies of the experimental model. Finally, we list the conclusions from this comparison.

Finite element method

Governing equations

The flow in the diffuser is treated as two-dimensional, incompressible, and steady. The governing equations are then the reduced Navier-Stokes equations and the continuity equation. The governing equations expressed in cylindrical coordinates are:

$$\frac{1}{r}\frac{\partial}{\partial r}(r\rho u)+\frac{1}{r}\frac{\partial}{\partial \theta}(\rho v)=0 \tag{1}$$

$$\rho u\frac{\partial u}{\partial r}+\rho v\frac{1}{r}\frac{\partial u}{\partial \theta}-\rho\frac{v^2}{r}=-\frac{\partial p}{\partial r}+\mu\left[\frac{1}{r}\frac{\partial}{\partial r}\left(r\frac{\partial u}{\partial r}\right)+\frac{1}{r^2}\frac{\partial^2 u}{\partial \theta^2}-\frac{u}{r^2}-\frac{2}{r^2}\frac{\partial v}{\partial \theta}\right] \tag{2}$$

* Department of Mechanical and Aerospace Engineering, University of Virginia, Charlottesville, VA 22901, USA

Received 11 December 1985 and accepted for publication 8 February 1987

0142-727X/87/030187-08$3.00

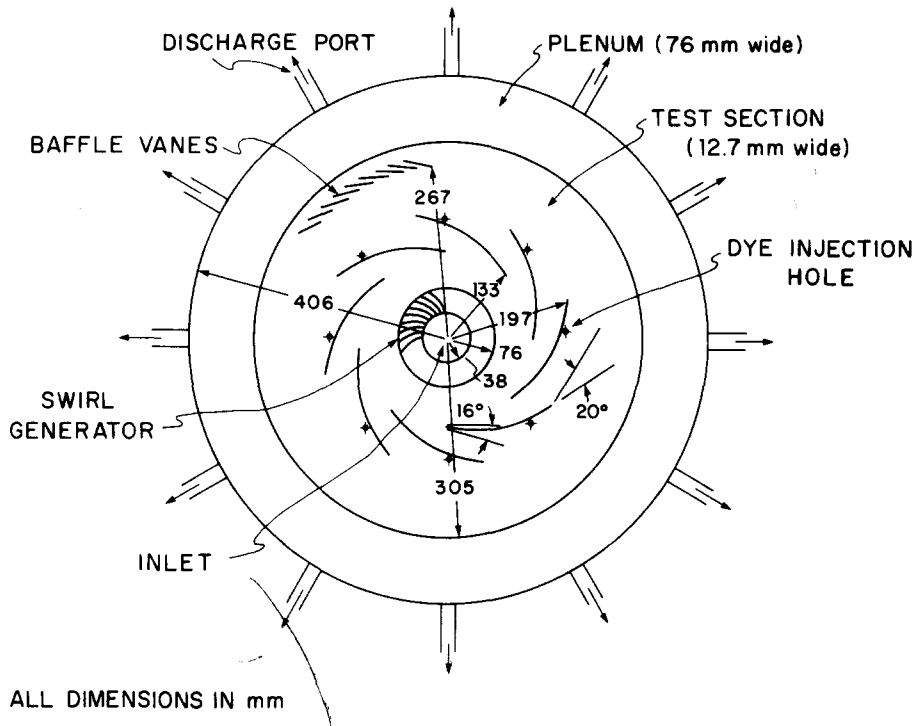

Figure 1 Exploded view of experimental diffuser model

$$\rho u\frac{\partial v}{\partial r}+\rho v\frac{1}{r}\frac{\partial v}{\partial \theta}+\rho\frac{uv}{r}=-\frac{1}{r}\frac{\partial p}{\partial \theta}$$
$$+\mu\left[\frac{1}{r}\frac{\partial}{\partial r}\left(r\frac{\partial v}{\partial r}\right)+\frac{1}{r^2}\frac{\partial^2 v}{\partial \theta^2}+\frac{2}{r^2}\frac{\partial u}{\partial \theta}-\frac{v}{r^2}\right] \quad (3)$$

The viscosity that appears in Equations 2 and 3 is the effective viscosity. A simple eddy viscosity turbulence model was used for this analysis. Since the primary interest in this analysis is flow visualization, a constant eddy viscosity was assumed, which turns out to be a reasonable first approximation for the type of flow considered.[2]

Finite element mesh

The solution domain is discretized using four node quadrilateral elements, as illustrated in Figure 2. Over each element, the dependent variables are approximated using bilinear shape functions of the form

$$\phi = ar + b\theta + cr\theta + d \quad (4)$$

Both velocity components and pressure are defined at the four indicated nodal locations on each element. No mixed-order approximation[3–5] (comparable to the staggered grid of finite differences[6]) is used.

Discretization

The two momentum equations are discretized using Galerkin's method following conventional finite element practice[7] for all terms except the advection terms, which are treated using the monotone streamline upwind approach described in Rice and Schnipke.[8]

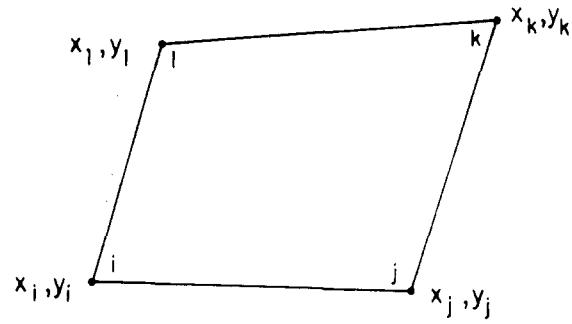

Figure 2 Four node quadrilateral element

In this approach, the advection terms for the transported variable, ϕ,

$$\rho u\frac{\partial \phi}{\partial r}+\rho v\frac{1}{r}\frac{\partial \phi}{\partial \theta} \quad (5)$$

are written in streamline coordinate as

$$\rho u_s\frac{\partial \phi}{\partial s} \quad (6)$$

where u_s is the streamwise velocity, and $\partial\phi/\partial s$ is the streamwise gradient of ϕ. Noting that for pure advection, ϕ is constant

Notation

A	Element area
a, b, c, d	Coefficients for polynomial shape function
a_{ij}^u	Coefficient matrix for u-momentum equation (Eq. 2)
a_{ij}^v	Coefficient matrix for v-momentum equation (Eq. 3)
f_i^u	Source term vector for u-momentum equation
f_i^v	Source term vector for v-momentum equation
p	Pressure, N/m^2
r	Radial distance, m
u	Radial velocity component, m/s
v	Circumferential velocity component, m/s
W	Weighting function
θ	Circumferential distance, radians
μ	Effective viscosity, kg/s · m
ρ	Mass density, kg/m^3
ϕ	General dependent variable

along a streamline, the terms like Equation 6 are treated as constants in the finite element residual equations for the transported variable ϕ. The values for Equation 6 are determined by a straightforward and inexpensive streamline tracing method.

The monotone streamline upwind approximation used here has been tested extensively on several standard or benchmark problems both in Cartesian[8,9] and cylindrical coordinates.[9]

The results from these problems demonstrate that the streamline upwind significantly reduces numerical diffusion but does not suffer from the overshoot-undershoot problem predominant in many of the discretization schemes designed to reduce numerical errors.[10-12]

The element residual equations are formed from the momentum equations as

$$\int\left\{\rho u\frac{\partial u}{\partial r}+\rho v\frac{1}{r}\frac{\partial u}{\partial\theta}-\rho\frac{v^2}{r}-\mu\left[\frac{1}{r}\frac{\partial}{\partial r}\left(r\frac{\partial u}{\partial r}\right)+\frac{1}{r^2}\frac{\partial^2 u}{\partial\theta^2}-\frac{u}{r^2}-\frac{2}{r^2}\frac{\partial v}{\partial\theta}\right]\right\}WdA=\int\left\{-\frac{\partial p}{\partial r}\right\}WdA \tag{7}$$

$$\int\left\{\rho u\frac{\partial v}{\partial r}+\rho v\frac{1}{r}\frac{\partial v}{\partial\theta}+\rho\frac{uv}{r}-\mu\left[\frac{1}{r}\frac{\partial}{\partial r}\left(r\frac{\partial v}{\partial r}\right)+\frac{1}{r^2}\frac{\partial^2 v}{\partial\theta^2}+\frac{2}{r^2}\frac{\partial u}{\partial\theta}-\frac{v}{r^2}\right]\right\}WdA=\int\left\{-\frac{1}{r}\frac{\partial p}{\partial\theta}\right\}WdA \tag{8}$$

Using Galerkin's method and the streamline upwind for the advection terms, these equations are evaluated over each element using a 2 × 2 Gauss quadrature. The element equations are then assembled to form the global node equations:

$$a_{ii}^u u_i=\sum_{j,j\neq i}a_{ij}^u u_j+f_i^u-\int\frac{\partial p}{\partial r}WdA \tag{9}$$

$$a_{ii}^v v_i=\sum_{j,j\neq i}a_{ij}^v v_j+f_i^v-\int\frac{1}{r}\frac{\partial p}{\partial\theta}WdA \tag{10}$$

The coefficient matrices a_{ij}^u and a_{ij}^v are identical, with the possible exception of different boundary conditions. Substituting the bilinear interpolation for pressure into Equations 9 and 10 results in the following global node equations:

$$a_{ii}^u u_i=\sum_{j,j\neq i}a_{ij}^u u_j+f_i^u+\sum_j b_{ij}^u p_j \tag{11}$$

$$a_{ii}^v v_i=\sum_{j,j\neq i}a_{ij}^v v_j+f_i^v+\sum_j b_{ij}^v p_j \tag{12}$$

Equations 11 and 12 are the discretized momentum equations that will be solved to determine u and v.

The pressure equation is derived element by element from the continuity equation. Since an equal-order bilinear approximation is used for the pressure, the continuity residual is formed by the product of the same weighting function as in the standard Galerkin formulation for the momentum equations. The element residual is

$$\int W\left\{\frac{1}{r}\frac{\partial}{\partial r}(r\rho u)+\frac{1}{r}\frac{\partial}{\partial\theta}(\rho v)\right\}dA \tag{13}$$

Integrate Equation 13 by parts to obtain

$$\int_s W\rho u r d\theta-\int_s W\rho v dr-\int\left\{\rho u\frac{\partial W}{\partial r}+\rho v\frac{1}{r}\frac{\partial W}{\partial\theta}\right\}rdrd\theta \tag{14}$$

Following conventional practice, the surface integral terms appearing in Equation 14 form the natural boundary conditions for the continuity equation or for the resulting pressure equation. These surface integrals will cancel along interior element surfaces when assembled, and they will be identically zero for either slip or no-slip wall boundaries. Hence they will contribute only at the inflow and outflow boundaries, providing a convenient means of specifying these boundaries conditions for the pressure.

The following integral then is evaluated over all elements:

$$\int\left\{\rho u\frac{\partial W}{\partial r}+\rho v\frac{1}{r}\frac{\partial W}{\partial\theta}\right\}rdrd\theta \tag{15}$$

At this point, the continuity equation residual defined by Equation 15 is expressed as a function of the velocity components u and v. To derive a pressure equation, a relation between velocity and pressure is required. This relation is obtained from the momentum equations as expressed in Equations 9 and 10.

As was successfully done in other finite difference methods,[6,13] assume the pressure gradients in Equations 9 and 10 are known. Then, in shorthand notation, these equations become

$$u_i=\hat{u}_i-K_u\frac{\partial p}{\partial r} \tag{16}$$

$$v_i=\hat{v}_i-K_v\frac{\partial p}{\partial\theta} \tag{17}$$

where

$$\hat{u}_i=\frac{\sum_{j,j\neq i}a_{ij}^u u_j+f_i^u}{a_{ii}^u} \tag{18}$$

$$\hat{v}_i=\frac{\sum_{j,j\neq i}a_{ij}^u v_j+f_i^v}{a_{ii}^v} \tag{19}$$

$$K_u=\frac{1}{a_{ii}^u}\int WdA \tag{20}$$

$$K_v=\frac{1}{a_{ii}^v}\int WdA \tag{21}$$

Equations 16 and 17 will serve as the required relation betwen the velocity and pressure. This relation is not exact but only an approximation. It is not essential, however, that this relation be exact for the iterative solution procedure to converge. This approximation is comparable to using a secant approximation in Newton's method.

Substituting Equations 16 and 17 into Equation 15 yields

$$-\int\int\rho\left(\hat{u}_i-K_u\frac{\partial p}{\partial r}\right)\frac{\partial W}{\partial r}rdrd\theta-\int\int\rho\left(\hat{v}_i-K_v\frac{\partial p}{\partial r}\right)\frac{\partial W}{\partial\theta}\frac{1}{r}drd\theta=0 \tag{22}$$

Equation 22 can be rearranged as

$$\text{zz Y}\quad oK_u\frac{\partial p}{\partial r}\frac{\partial W}{\partial r}r+\rho K_v\frac{1}{r}\frac{\partial p}{\partial\theta}\frac{\partial W}{\partial\theta}\Big]drd\theta=\int\int\left[\rho\hat{u}_i\frac{\partial W}{\partial r}r+\rho\hat{v}_i\frac{1}{r}\frac{\partial W}{\partial\theta}\right]drd\theta \tag{23}$$

Equation 23 is the resulting pressure equation. It is a Poisson type equation and therefore results in a symmetric positive definite coefficient matrix. Unlike other Poisson pressure equations,[14] Equation 23 was derived from the continuity equation and thus contains a direct continuity constraint.

With the pressure established by Equation 23, the velocities are updated using the algebraic relations:

$$u_i=\hat{u}_i+\sum_j b_{ij}^u p_j \tag{24}$$

$$v_i=\hat{v}_i+\sum_j b_{ij}^v p_j \tag{25}$$

where the hat velocities are defined by Equations 18 and 19.

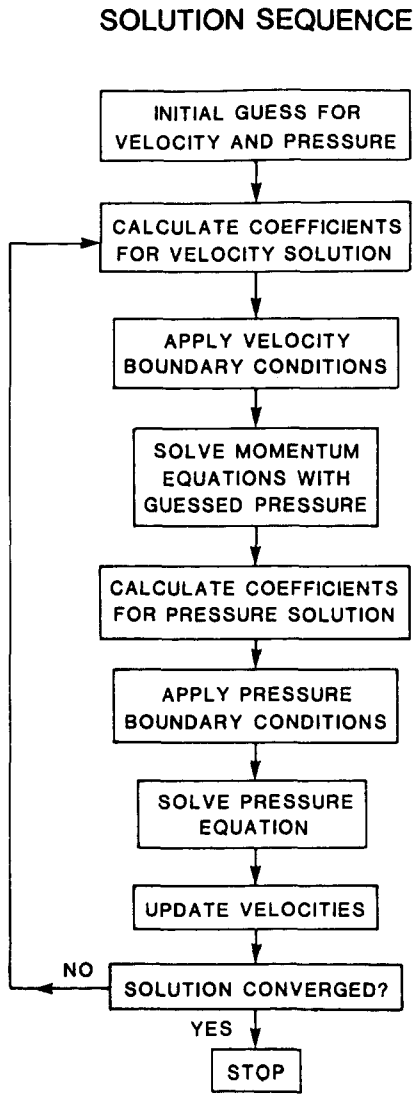

Figure 3 Overall solution organization

Segregated solution

The overall organization of the iterative solution strategy is illustrated in Figure 3. As shown, the solution is a segregated approach where the two velocity components and pressure are solved for sequentially rather than simultaneously. Most previous finite element formulations use a direct solution method and simultaneously solve for all three variables. The use of the segregated approach, common in finite difference methods, results in a considerable savings in coefficient storage and execution time.

The solution of the discretized equations for momentum and pressure is accomplished using iterative solution methods. These do not require the storage of the global matrices in banded form. Only the nonzero terms are stored along the lines of many finite difference methods. The required computer storage is then a linear function of the number of nodes and is independent of the bandwidth of the matrix.

Iterative solution methods

The algebraic equations for the nodal pressure values are solved using a preconditioned conjugate gradient (PCG) solution method[15,16]. The current calculations used incomplete Cholesky decomposition for the preconditioning step. The PCG solution method is semidirect[15] and provides a very accurate and rapid solution of the pressure equation without the prohibitive storage requirements of a direct solution method such as Gaussian elimination. The PCG solution method is also much faster than direct methods for large two-dimensional or, in particular, three-dimensional problems. This particular method is applicable only to symmetric matrices and thus was used only for the pressure equation (Equation 23) and not the nonsymmetric momentum equations. The momentum equations (Equations 11 and 12) are solved using a tridiagonal approximate factorization.

Boundary conditions

The boundary conditions used for both geometries analyzed were similar, except for the number of nodes specified.

Inlet boundary

Along the inner radius or inlet boundary, both inlet velocity components were specified. The magnitude of the radial inlet velocity was specified to match the experimental flow rate as given in Brownwell *et al.*[1] The tangential velocity component was then specified accordingly to provide the prescribed inlet flow angle. Both the radial and tangential velocity were taken to be uniform over the inlet. The pressure boundary condition was obtained by calculating the surface integrals in Equation 14 using these specified velocities.

Exit boundary

At the outer radius or exit boundary, a specified constant pressure and flow angle were specified. The formulation does not require that the flow angle be specified. However, the experimental model has a large number of turning vanes at the outlet.[1] To simulate these vanes, the flow angle was specified in the following manner. Natural boundary conditions were used for the radial velocity component. The tangential velocity component was then calculated from the following relation:

$$v = u \tan \theta_e \tag{26}$$

where θ_e is the prescribed exit flow angle.

Periodic boundaries

The treatment of the periodic boundary conditions yields nodal equations for nodes lying on the periodic boundaries identical in form to an interior node in the solution domain. From a computational viewpoint, these nodes are not boundary nodes.

Figure 4 illustrates a pair of periodic boundaries. Nodes 3 and 18 form a pair of periodic nodes. The treatment essentially involves a modification of the assembly procedure. In the modified assembly procedure, the contributions from elements *A and B* are assembled as contributions to the global equation for node 3. The resulting global equation for node 3 has the stencil indicated in Figure 4. Moreover, all references to node 18 are eliminated from the global equations. In the solution of the global equation, the value for node 3 is actually determined. Following this solution, the nodal value for node 18 is then updated. This procedure is used for all variables.

Blade boundary

On the blade surface, both velocity components were set to zero, no-slip wall boundaries.

Problem geometry

The experimental diffuser rig model is shown in Figure 5. For a more complete description of the geometry, see Reference 1. Water enters the diffuser through the inner radius at a blade angle of 16° and leaves through the outer radius at the same angle. The diffuser was modeled with four and eight blades at Reynolds number of approximately 20,000.

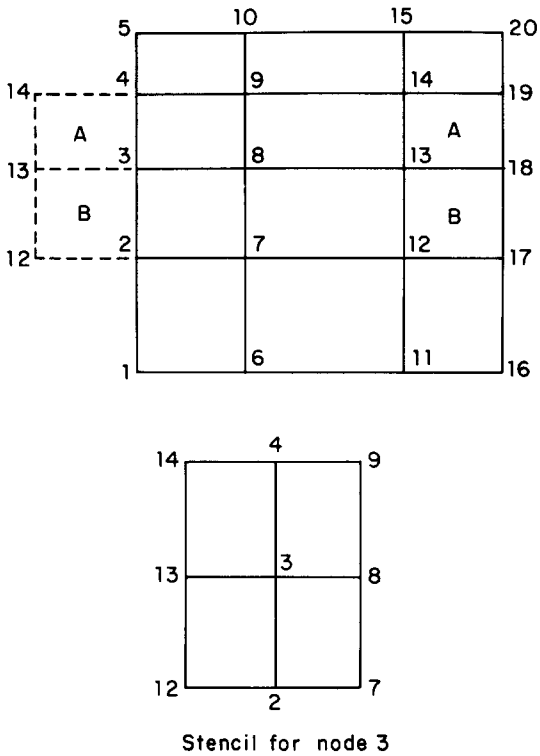

Figure 4 Periodic boundaries

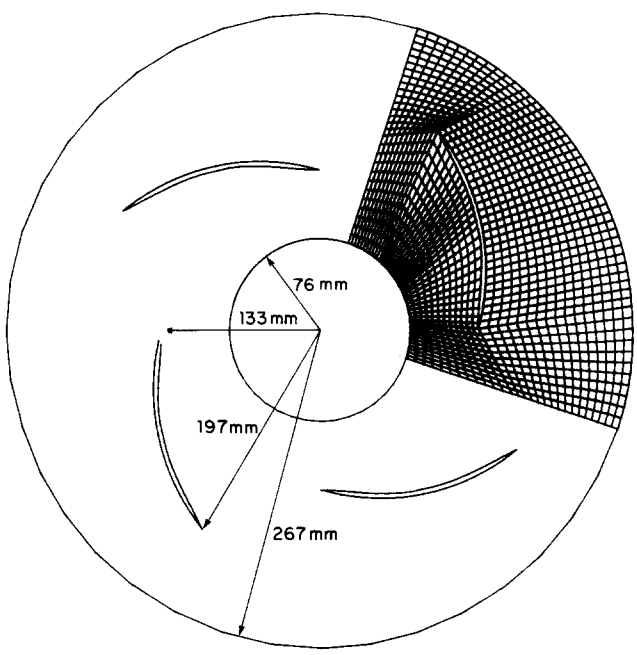

Figure 5 Four blade vaned diffuser model

Because of the symmetry of the problem, only a portion of the diffuser was modeled. For the four blade model, one fourth of the geometry was discretized, as shown in Figure 5. The two outer radial lines of the discretized region are treated using the periodic boundary conditions described previously. This quadrant could have been chosen anywhere in the diffuser. This analysis used 1467 nodes and 1364 elements.

One eighth of the eight blade diffuser was modeled, as shown in Figure 6. Nodes along the radial lines marked I1 and I2 form the inner periodic pairs of nodes. Nodes along the radial lines marked O1 and O2 form the outer periodic pairs of nodes. The lines between blades 4 and 5 illustrate how the discretized region was generated. Each of these four sided regions is subdivided into elements using an isoparametric mapping approach.[17] These four regions were selected to minimize the number of long tapered elements. This analysis required 1215 nodes and 1120 elements.

Both geometries were analyzed using coarser meshes. The number of elements were increased until the separation points did not change more than 10% from the coarser mesh and the size and shape of the recirculation regions were unchanged.

Results

Computed results of the four blade diffuser analysis are shown in Figures 7–10. Figure 7 shows the streamlines of the flow, and Figure 8 is a plot of the velocity vectors. These figures show that the flow separates from the pressure side of the blade very early. The predicted separation point occurs at 19.6% of the blade length from the leading tip. The experimentally observed value was 23%.

Figures 7 and 8 also indicate that very little flow enters the recirculation region. Velocities in this region are two orders of magnitude less than in the jet near the leading edge of the blade. Figure 9, the unscaled velocity vectors (similar to a yarn tuft photograph[1]), shows two counterrotating vortices are in this recirculation region. The vortices are broken by one periodic boundary and continue on the other. Figures 7–9 also show clearly the effect of the turning vanes at the exit of the diffuser is restricted to the first few nodes in from the exit.

Figure 10 shows the pressure contours for the four blade diffuser. As a result of the large recirculation area on the pressure side of the blade, all the pressure recovery occurs on the suction side. The pressure contours as well as the streamlines exhibit a near potential flow behavior on this suction side. The stagnation point at the leading edge of the blade is also clearly visible. In general, the flow patterns predicted agree qualitatively with what was observed experimentally.

The results of the eight blade diffuser analysis are shown in Figures 11–14. Figure 11 is a plot of the streamlines of the flow, and Figure 12 shows the velocity vectors. These two figures demonstrate that the effect of the additional blades was to delay separation. For this case, the predicted separation point occurs at 43% of the blade length from the leading tip. Experimentally, this value was determined as 50%.

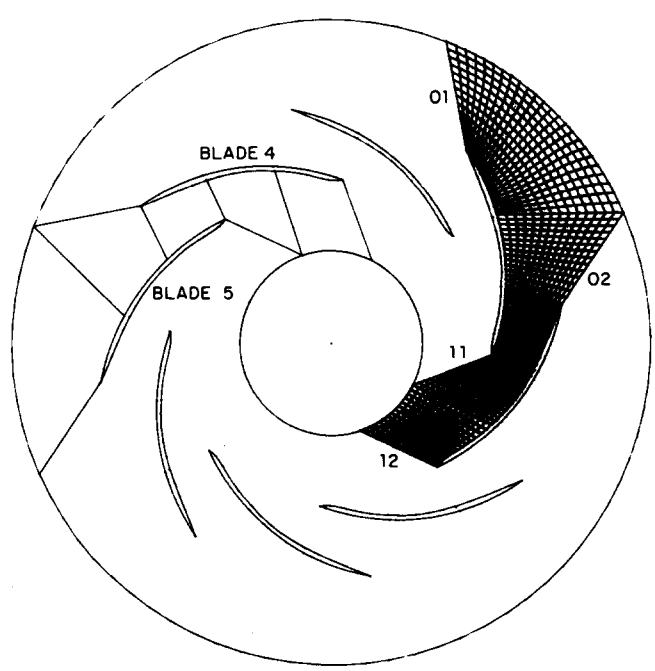

Figure 6 Eight blade vaned diffuser model

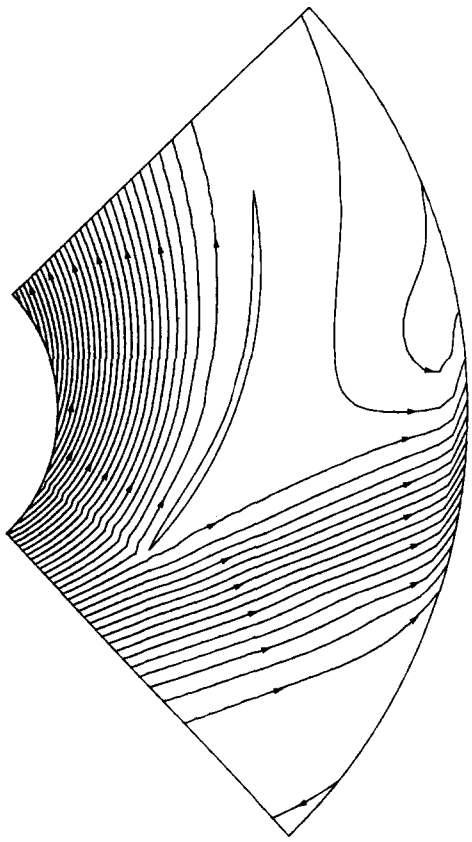

Figure 7 Streamlines for four blade diffuser

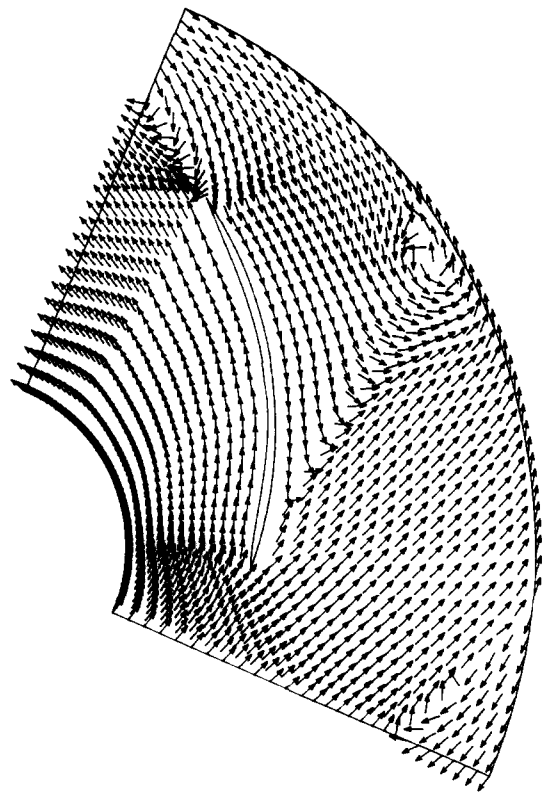

Figure 9 Unscaled velocity vectors for four blade diffuser

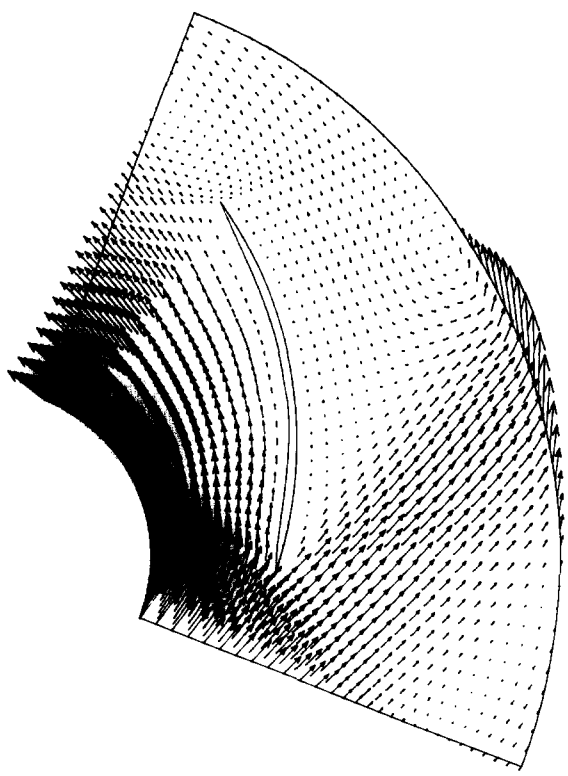

Figure 8 Scaled velocity vectors for four blade diffuser

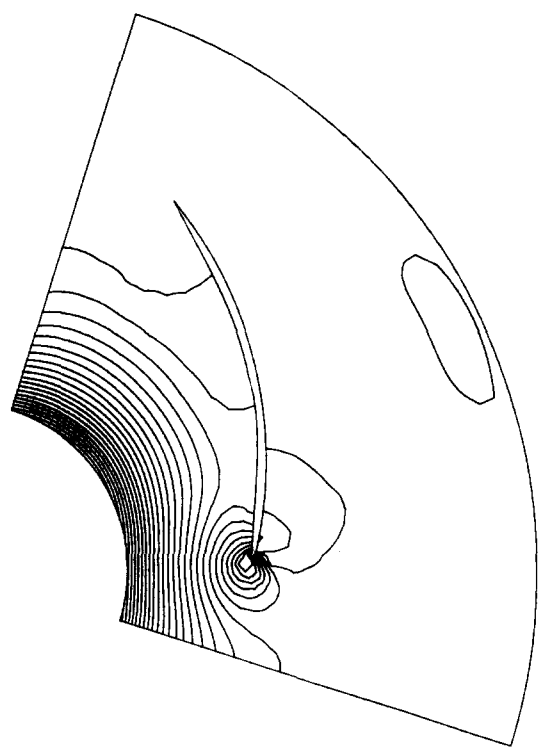

Figure 10 Pressure contours for four blade diffuser

Figures 11 and 12 also show little flow enters the recirculation region. However, the velocities in this wake region are only one order of magnitude less than the jet velocities. These two figures do show the two counterrotating vortices in the recirculation region. However, the unscaled velocity vectors in Figure 13 point out a third smaller vortex near the separation point. Again, vortices that get broken by one periodic boundary continue on the paired periodic boundary. As for the four blade case, the exit turning vanes affect only a narrow region just before the diffuser exit.

Figure 14 shows the pressure contours from the eight blade diffuser analysis. Like the four blade model, all the pressure recovery lies beneath the blades. In fact, for the eight blade case, a significant portion of the recovered pressure is lost again

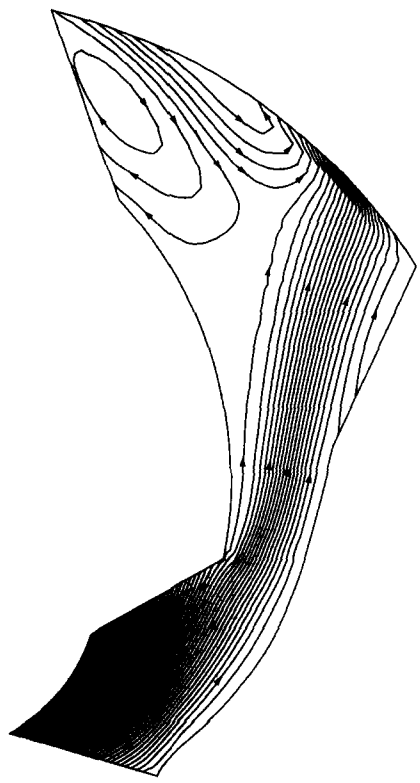

Figure 11 Streamlines for eight blade diffuser

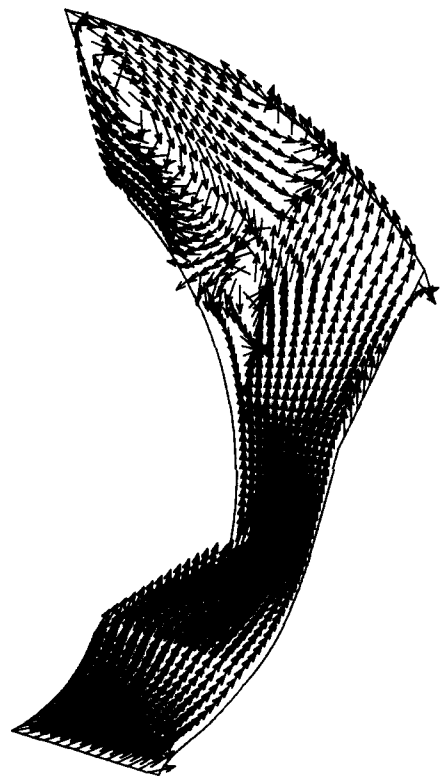

Figure 13 Unscaled velocity vectors for eight blade diffuser

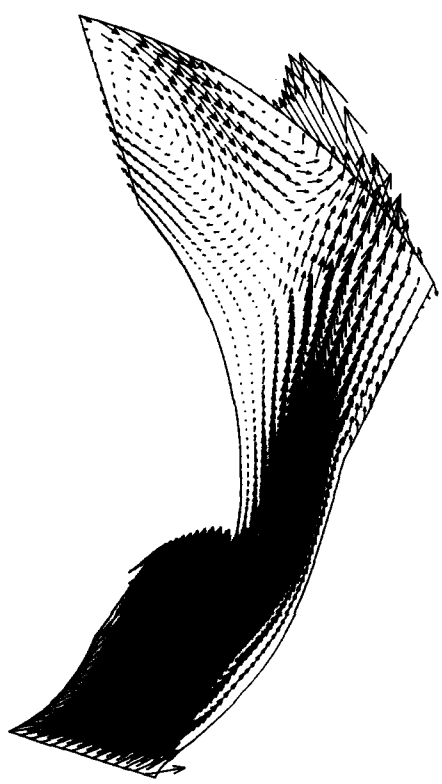

Figure 12 Scaled velocity vectors for eight blade diffuser

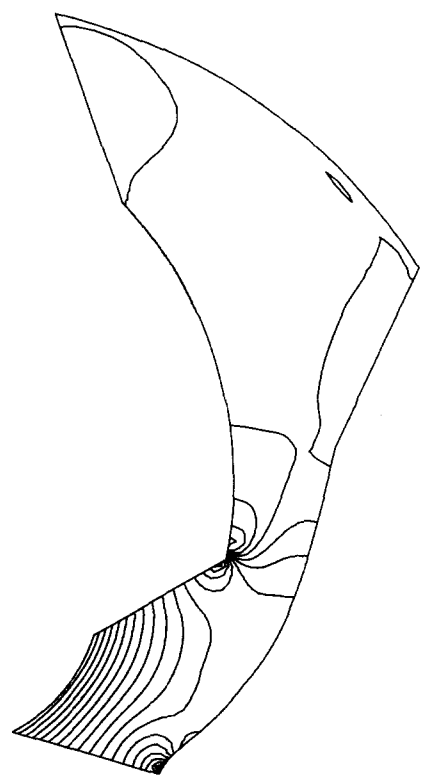

Figure 14 Pressure contours for eight blade diffuser

between the blades. Again, the flow patterns predicted agree qualitatively with experimental observations.

Both analyses were performed on a Prime 850 computer. The four blade solution required 150 iterations to achieve a converged solution with an average change in pressure of less than 0.1%. Total CPU time for this analysis was 324 minutes. The eight blade solution required 125 iterations to achieve a converged solution with the average pressure change less than 0.1%. Total CPU time for this analysis was 272 minutes. For this computer, these numbers are comparable to the CPU requirements of many of the available finite difference methods.

Conclusions

A new finite element method was used to analyze a laboratory vaned diffuser. This experimental diffuser contained many of the

complex features common to practical turbomachinery problems, including steep pressure and velocity gradients and separating flow. The separation point predicted by this method for the four blade diffuser occurred at 19.6% of the blade length from the blade leading edge. Experimentally, separation occurred at 23% of the blade length. For the eight blade diffuser, the predicted separation point was 43% of the blade length from the leading edge. The experimentally observed value was 50%. In general, the predicted flow patterns agreed with experimental observations. This comparison indicates that the numerical method presented here is a reliable technique for predicting complex fluid flows.

The current finite element method has also been demonstrated to be competitive in required storage and execution times with available finite difference methods.

This analysis method has recently been extended to include three-dimensional modeling capability. Early benchmark runs indicate that this finite element method has the same order of magnitude cycle time as a comparable finite difference method.

Acknowledgement

This work was sponsored by the Rotating Machinery and Controls (ROMAC) Industrial Research Program at the University of Virginia.

References

1 Brownell, R. B., Flack, R. D., Davis, M. C., and Rice, J. G. Flow visualization in a laboratory vaned diffuser. *Int. J. Heat and Fluid Flow*, 1987, **8**, 37–43.

2 Monin, A. S., and Yaglom, A. M. *Statistical Fluid Mechanics: Mechanics of Turbulence*. M.I.T. Press, Cambridge, Mass., 1971.

3 Donea, J., Giuliani, S., Morgan, K., and Quartapelle, L. The significance of chequerboarding in a Galerkin finite element solution of the Navier-Stokes equations. *Int. J. Numer. Methods Eng.*, 1981, **17**(5), 790–795.

4 Sani, R. L., Gresho, P. M., Lee, R. L., and Griffiths, D. F. The cause and cure of the spurious pressures generated by certain FEM solutions of the incompressible Navier-Stokes equations: part 1. *Int. J. Numer. Methods Fluids*, 1980, **1**, 17–43.

5 Baliga, B. R., and Patankar, S. V. A control volume finite-element method for two-dimensional fluid flow and heat transfer. *Numer. Heat Transfer*, 1983, **6**, 245–261.

6 Patankar, S. V. *Numerical Heat Transfer and Fluid Flow*. Hemisphere, New York, 1980.

7 Allaire, P. E. *Basics of the Finite Element Method*. Wm. C. Brown, Dubuque, Iowa, 1985.

8 Rice, J. G., and Schnipke, R. J. A monotone streamline upwind finite element method for convection-dominated flows. *Computer Methods in Appl. Mech. Eng.*, 1985, **48**, 313–327.

9 Schnipke, R. J. A streamline upwind finite element method for laminar and turbulent flow. PhD dissertation, University of Virginia, May 1986.

10 Smith, R. M., and Hutton, A. G. The numerical treatment of advection: a performance comparison of current methods. *Numer. Heat Transfer*, 1982, **5**, 439–461.

11 Patel, M. K., Markatos, N. C., and Cross, M. A critical evaluation of seven discretization schemes for convection-diffusion equations. *Int. J. Numer. Methods in Fluids*, 1985, **5**, 225–244.

12 Huang, P. G., Launder, B. E., and Leschziner, M. A. Discretization of nonlinear convection processes: a broad-range comparison of four schemes. *Computer Methods in Appl. Mech. Eng.*, 1985, **48**, 1–24.

13 Raithby, G. D., and Schneider, G. E. Numerical solution of problems in incompressible fluid flow: treatment of the velocity-pressure coupling. *Numer. Heat Transfer*, 1979, **2**, 417–440.

14 Schneider, G. E., Raithby, G. D., and Yovanovich, M. M. Finite-element solution procedures for solving the incompressible, Navier-Stokes equations using equal order variable interpolation. *Numer. Heat Transfer*, 1978, **1**, 433–452.

15 Lange, R. R., and Rice, J. G. On the use of the preconditioned conjugate gradient methods for finite element equations. Submitted to *Int. J. Numer. Methods in Fluids*, 1985.

16 Kershaw, D. The incomplete Cholesky conjugate gradient method for the iterative solution of systems of linear equations. *J. Computational Physics*, 1978, **26**, 43–65.

17 PDA Engineering. *PATRAN-G User's Manual*.